JOURNAL OF GEOPHYSICAL RESEARCH, VOL. 114, D00E08, doi:10.1029/2008JD010641, 2009

Cloud, thermodynamic, and precipitation observations in West Africa during 2006

Pavlos Kollias,[1] Mark A. Miller,[2] Karen L. Johnson,[3] Michael P. Jensen,[3] and David T. Troyan[3]

Received 20 June 2008; revised 17 February 2009; accepted 10 March 2009; published 27 June 2009.

[1] In 2006, the ARM Mobile Facility (AMF) completed a 1-year deployment at Niamey, Niger, Africa, in support of the Radiative Atmospheric Divergence using ARM Mobile Facility, GERB data and AMMA Stations (RADAGAST) field campaign, which is the subject of this special issue. Observations from the AMF instrumentation are used to analyze the relationship between clouds, precipitation, and the thermodynamic environment in this rarely observed region and to evaluate the cloud fields in the National Center for Environmental Prediction Global Forecast System (GFS) initialization product. The 1-year deployment period enabled measurements in the dry and wet (monsoon) seasons and through the transitions in May and September, respectively. Cirrus clouds in the 10- to 15-km layer with modest monthly cloud fraction and mean depth of ~1 km are ubiquitous through the observing period as observed in other regions of the tropics. The monsoon season from May to September is characterized by convective clouds of varying depth that produce precipitation of varying intensity, as indicated by cloud radar. Peak surface rainfall is observed during August, and the largest daily rainfall rates are observed during the period from July to September. The lifting condensation level (LCL) is observed to decrease as the monsoon season progresses, and a strong correlation between the height of the LCL and precipitation is demonstrated. Cooling of the lower troposphere is implicated as the probable cause of the lowering of the LCL. Conversely, the amount of convective available potential energy is found to be poorly correlated with precipitation. As in other tropical regions, the physical height at which the zero-degree isotherm is observed corresponds to gradients in the thermodynamic profiles and a gradient in the profile of cloud occurrence. Comparisons with the GFS initialization data, which are derived from a number of sources including satellites, show some systematic biases when compared to AMF measurements. There is general correspondence between the locations of clouds and the profile of vertical velocity diagnosed by the GFS initialization early in the monsoon season, but vague correspondence thereafter. The relative humidity in the GFS initialization is too large above 10 km and too small in the monsoon layer near the surface, and it seriously underestimates the amount of cloud below 10 km during August, which is the height of the West African monsoon in Niamey.

Citation: Kollias, P., M. A. Miller, K. L. Johnson, M. P. Jensen, and D. T. Troyan (2009), Cloud, thermodynamic, and precipitation observations in West Africa during 2006, *J. Geophys. Res.*, *114*, D00E08, doi:10.1029/2008JD010641.

1. Introduction

[2] The Sahel region of West Africa has experienced recurring and persistent precipitation anomalies for at least the past 50 years. Periodicity on the scale of a decade or more is common and severe droughts have caused extreme societal consequences. A plethora of mechanisms have been proposed to explain precipitation anomalies [*Desbois et al.*, 1988]. Such mechanisms include feedbacks from changes in surface albedo and soil moisture [*Otterman*, 1974; *Charney*, 1975] and periodic shifts in the large-scale dynamic construct of the region related to the African easterly jet and sea surface temperatures in the tropical Atlantic [*Lamb*, 1978; *Cook*, 1999].

[3] The bulk of the rainfall that is observed in the Sahel is associated with propagating mesoscale convective complexes and tropical squall lines [*Laing and Fritsch*, 1993; *Desbois et al.*, 1988]. Several studies have used satellite climatology to show that these storm complexes often propagate from east to west across the Sahel and are

[1]Department of Atmospheric and Oceanic Sciences, McGill University, Montreal, Quebec, Canada.
[2]Department of Environmental Sciences, Rutgers University, New Brunswick, New Jersey, USA.
[3]Department of Atmospheric Sciences, Brookhaven National Laboratory, Upton, New York, USA.

0148-0227/09/2008JD010641$09.00

often associated with tropical easterly waves. Satellite data have also been used to examine the characteristics of easterly waves, the structure of precipitation-producing complexes, and climatology and diurnal cycle of clouds in the region. Other studies have employed model data assimilation techniques used in the initialization of numerical models to characterize the thermodynamic, cloud, and wind fields over West Africa [*Thorncroft and Haile*, 1995], and to relate them to precipitation anomalies.

[4] The sparse amount of data available from West Africa has often proved a significant limitation in past studies. Cloudiness is often characterized using its infrared cloud top temperature or visible detection, which limits the resolution of underlying clouds. Such techniques are used in the National Center for Environmental Prediction Global Forecast System (GFS) initialization product. Radiosonde profiles are relatively infrequent in the region. Past studies have made significant strides, but there is still considerable uncertainty as to the details of cloud cover and precipitation, and its relationship with the thermodynamic structure over West Africa.

[5] The purpose of this paper is to present a detailed assay of cloud and thermodynamic structure over a portion of West Africa with unprecedented rigor, and the monsoon season (May through September) is studied with particular emphasis. The data were collected using the United States Department of Energy's Atmospheric Radiation Measurement (ARM) Mobile Facility (AMF), which is a portable atmospheric laboratory. It is equipped with a suite of instruments designed to collect vertically resolved measurements of the structure of the troposphere in cloudy and clear atmospheres in undersampled regions. From January 2006 to January 2007, the AMF completed a year-long international deployment in Niamey, Niger, West Africa, at the Niger Meteorological Office at Niamey International Airport (N13°28.638′, E2°10.547′, 205 m). Niamey and the balance of sub-Saharan Africa straddle the region between the migrating Intertropical Convergence Zone (ITCZ), which is one of the wettest locations on the planet, and the Sahara desert, which is one of the driest. This location between planetary moisture extremes separated by a relatively small distance suggests that Niamey lies within one of the largest moisture gradients on Earth.

[6] The AMF deployment [*Miller and Slingo*, 2007] was timed to coincide with the field phases and Special Observing Periods of the African Monsoon Multidisplinary Analysis (AMMA) [*Lebel et al.*, 2003] and the Geostationary Earth Radiation Budget (GERB) [*Harries et al.*, 2005] experiment. ARM participated in this international effort as part of the Radiative Divergence using AMF, GERB and AMMA Stations (RADAGAST) field campaign. The primary purpose of the RADAGAST AMF deployment was to provide continuous measurements of the broadband upward and downward solar and thermal broadband radiative fluxes at the surface that could be combined with the corresponding measurements from GERB to estimate the radiative divergence across the atmosphere [*Slingo et al.*, 2006; *Miller and Slingo*, 2007].

[7] The AMF sampled a variety of conditions during its deployment and captured the annual and diurnal cycles of precipitation and cloudiness in the atmospheric column above Niamey. Time series and statistical analyses of these data are used in the sections that follow to examine the vertical structure of clouds and the connections between the thermodynamic profile and precipitation.

2. Methodology

[8] The general approach taken here is to analyze the vertical profile of cloudiness in the column above Niamey using surface-based remote sensors and the accompanying thermodynamic environment using an assimilation procedure. The assimilated product is based upon radiosonde ascents every 3 hours from Niamey International Airport complemented by a regional diagnosis of the thermodynamic state from a model. This approach enables specific features within the vertical profile of cloud structure to be related to specific thermodynamic features.

[9] The AMF baseline suite of instruments used in this study include a 94-GHz (W-band) ARM cloud radar (WACR), a two-channel Microwave Radiometer (MWR), a twelve-channel Microwave Radiometer Profiler (MWRP), a micropulse lidar (MPL), a ceilometer, and surface meteorology. A cloud radar receives echoes from nonprecipitating and lightly precipitating clouds (Figure 1) and observations from the WACR are available after mid-April 2006 owing to late arrival of the newly fabricated radar in Niamey relative to other instrumentation. Continuous observations with the WACR were collected until the end of the deployment (end of 2006). A limitation of the WACR is that its beam suffers attenuation when it traverses shafts of heavy precipitation that are often associated with deep convection. This attenuation may cause the WACR to record erroneously low cloud tops (Figure 1) when heavy precipitation is observed.

[10] WACR Doppler moments and linear depolarization ratios (LDRs) were combined with MPL backscatter measurements and ceilometer cloud base heights to provide a cloud and precipitation mask and cloud boundaries with a temporal resolution of 5 s and vertical resolution of 45 m. The basic approach adopted for this instrument synthesis is similar to that used in ARM's Active Remote Sensing of CLouds (ARSCL) [*Clothiaux et al.*, 2000] instrument merging product, which is based on 35-GHz Millimeter Cloud Radar observations rather than the 94-GHz WACR frequency. First, an MPL-based cloud mask is developed by comparing lidar backscatter measurements with returns during known clear sky periods. The MPL cloud mask is combined with ceilometer cloud base measurements to produce a best-estimate cloud base for each time period. Next, a WACR hydrometeor mask (cloud and precipitation) is derived on the basis of signal-to-noise-ratio thresholds, which are determined for each time profile. The MPL and WACR cloud masks are then merged to take advantage of each instrument's strengths. For example, the radar signal is able to detect cloud tops, penetrating thick cloud layers that attenuate the MPL signal, while the MPL is sensitive to very thin cloud layers that elude WACR detection.

[11] Additional filtering of the merged WACR/MPL cloud mask is applied in the lower troposphere (below approximately 3.5 km) to flag probable insect returns. The linear depolarization ratio (LDR) is used as the primary insect filter criterion because depolarization of a polarized transmitted pulse occurs when the target has an irregular

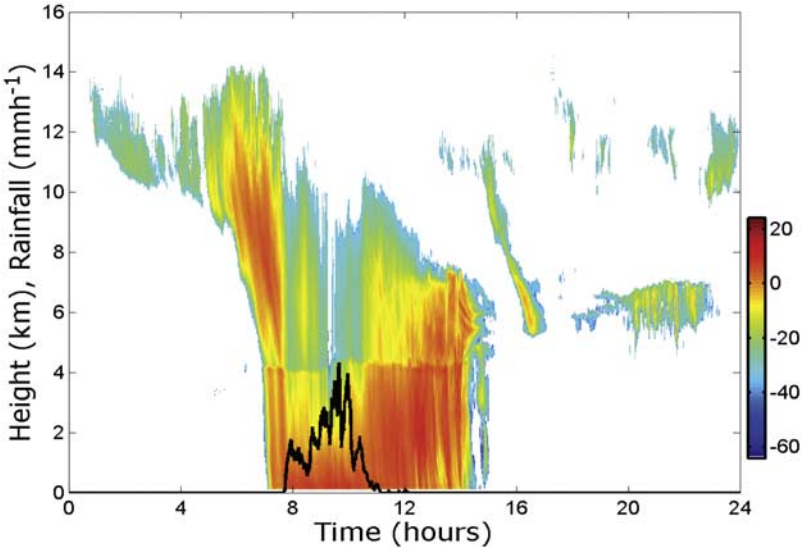

Figure 1. Example of 94-GHz cloud radar reflectivity on 8 August 2006 at Niamey, Niger, during the AMF deployment. The black line indicates the tipping bucket surface rainfall rate in mm h^{-1}.

shape. Insects, typically nonspherical, produce LDR returns that are significantly larger than spherical cloud droplets. Boundary layer returns with relatively high LDR, but low reflectivity (hence not likely to be associated with large oblate precipitation targets), were flagged as insect-contaminated and removed from the hydrometeor mask.

[12] The cloud and precipitation mask, the cloud layer boundaries time series, and the recorded surface rainfall rate at the AMF site are used as input to a cloud and precipitation classification scheme. This scheme generates hourly estimates of cloud fraction, cloud base height, and cloud thickness for various cloud types. Cirrus clouds are defined as clouds with bases above 7 km, middle clouds as those having bases between 3 and 7 km, and boundary layer clouds as those having tops below 3 km.

[13] One goal of the precipitation scheme is to determine the fraction of time during which there is liquid precipitation in the column and whether it reaches the surface in measurable quantity or not. Precipitation reaching the surface is identified and flagged when the reflectivity is greater than 0 dBZ in the lowest two radar measurement heights or it is detected by the tipping bucket rain gauge. Precipitation not reaching the surface (virga) is identified and flagged when there is a cloud base in the 0 to 200 m range coupled with a cloud top above 3 km and a reflectivity of −17 dBZ or more within the lowest 5.5 km [*Frisch et al.*, 1995]. For comparison, the hourly fraction of measurable surface precipitation (rainfall > 0.245 mm h^{-1}, which is the measurement threshold) is estimated using a tipping bucket rain gauge.

[14] A second goal of the precipitation scheme is to identify periods when the WACR may be experiencing significant attenuation of its transmitted pulses by rainfall. This attenuation may prevent transmitted pulses from reaching cloud top or diminish their power content to a level that prohibits the detection of an echo. Such attenuation is indicated by an artificial reduction in the measured cloud top height (Figure 1) at the time of maximum precipitation rate in the column.

[15] The environmental thermodynamic profile is measured at 3-h intervals using Vaisala RS-92 radiosondes. To circumvent the scale discordance between variability in the cloud field, which typically occurs on a scale of less than one-half hour, a data assimilation technique was created to estimate the thermodynamic profile at times between radiosonde launches. Radiosonde data are assimilated with surface-based meteorology and model-produced profiles from the European Centre for Medium Range Weather Forecasting (ECMWF) [*Jensen and Troyan*, 2006]. The ECMWF fields are expected to contain information about structural changes between radiosonde ascents because it is initialized with spatial information from the surrounding radiosonde network in West Africa. To assimilate the two thermodynamic fields, a temporal weighting function is applied to the radiosonde profile that gives it 100% weighting to the sonde observations at the observation time and height with steadily declining weight during the hour and a half before and after the observation time. As a matter of general course, the column integrated water vapor in the merged product is adjusted to agree with that measured by the MWR.

3. Results

[16] The analysis below comprises two components: an analysis of the seasonal and monthly distribution of cloud cover and an analysis of this structure in the context of the local thermodynamic environment during the monsoon. In the latter analysis, efforts are made to determine the links between observed precipitation and the characteristics of the cloud and thermodynamic fields.

3.1. Cloud and Precipitation Statistics

[17] During the October to April period (dry season), the lower atmosphere in Niamey has little cloud cover and high concentrations of dust blown from the Sahara Desert and aerosol from local and regional biomass burning. From May to September (wet season), the onset and end of the

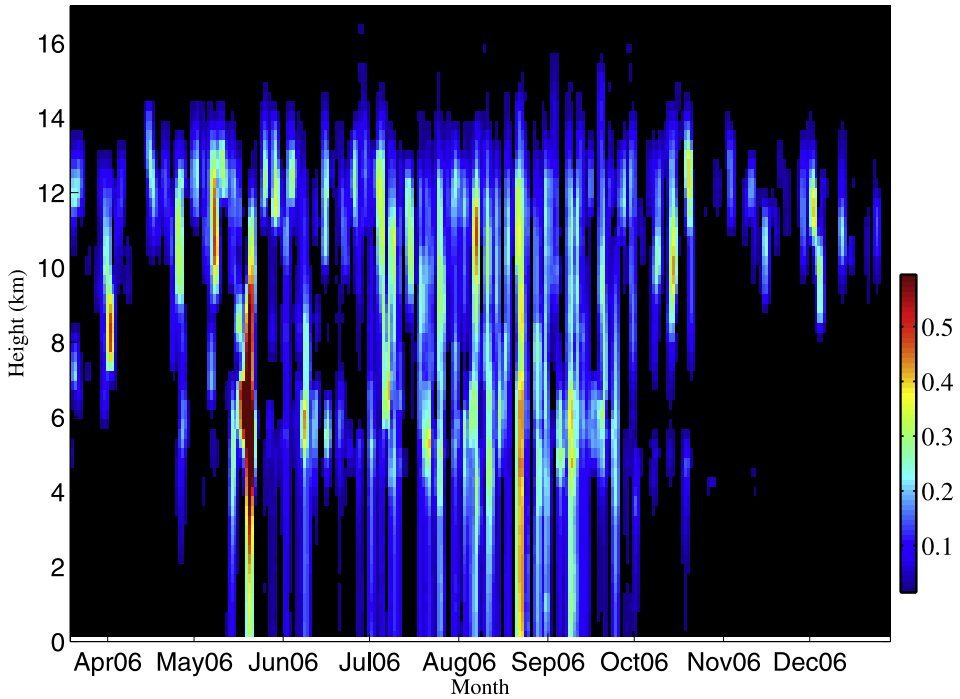

Figure 2. Daily observed cloud fraction in Niamey during the AMF deployment. The cloud fraction is derived from measurements from the 94-GHz radar, the micropulse lidar, and the ceilometer. The vertical resolution is 260 m, and a 5-day temporal average is applied to the daily cloud fraction profiles.

precipitation cycle is observed as indicated by the extension of the 94-GHz radar echoes to the surface in association with falling precipitation (Figure 2). The wet season is characterized by convection of varying depth and intensity ranging from large, organized mesoscale complexes that generate severe weather and heavy rainfall to weakly or nonprecipitating cumulus. The convection during the wet season occurs on a regular basis often coming in periods of enhancement, hereafter termed bursts, which may last for several days. These bursts are indicated (Figure 2) by the coherent vertical structures surrounded by regions with zero cloud fraction present in the cloud fraction profiles. These convective bursts last a few days and extend through the full depth of the troposphere at times, particularly during the rainy season. They also manifest themselves as disconnected peaks at two or more separate levels during the same time period, as in October for example.

[18] The most frequently observed cloud type through the seasonal cycle is cirrus in the layer between approximately 10 and 15 km, which persists in both the dry and wet seasons (Figures 2 and 3). A strongly resilient cirrus layer is frequently observed over tropical oceans [*Comstock et al.*, 2002] and may be a prominent component of the continental tropical environment over West Africa if this nearly year-long cloud radar data set is representative. The onset of the monsoon in Niamey is characterized by the passage of the ITCZ. The periods of deep, strong radar echoes in mid-May and August mark the passage of the ITCZ during the study period.

[19] Cirrus daily observed cloud fraction is generally less than 10% (November–December) in the dry season and increases to nearly 20% during the apex of the wet season (July and August; Figure 3). Boundary layer clouds that are reflective enough to be detected by the cloud radar are virtually nonexistent during the dry season (monthly mean cloud fraction $\sim$ 1–2%) and relatively infrequent during the wet season (monthly mean cloud fraction 10% or less). This may be due to the relative dryness of air from the Sahara, which is often found above a shallow moist layer as will be shown later. Relative to low and high clouds, midlevel cloudiness exhibits a strong seasonal cycle in monthly mean cloud fraction (1–5% in dry season, 20–25% in wet season). The seasonal fluctuation in midlevel cloudiness is due to the emergence of deep convection during the monsoon season and, as will be shown subsequently, a peak in midlevel cloudiness at the freezing level.

[20] The deployment-average profile of cloud and precipitation fraction (Figure 3b) exhibits a bimodal structure with a maximum of 10% at 11.5 km (cirrus clouds) and a secondary peak (7.5%) at 5.5 km. This secondary peak in cloud fraction lies in proximity to the freezing level encountered by developing convective clouds, which will be shown subsequently. During the wet season, the peak is located 1–1.5 km. above the melting layer for falling precipitation, which typically occurs below the freezing level because it takes time for the phase change from ice to liquid to occur. This phase change is characterized by a localized maximum in radar reflectivity known as the radar bright band, which occurs partly as a consequence of the collapse of melting snowflakes into a central core of ice coated with spherical surface of liquid water. The low-density ice core exaggerates droplet size when compared to a droplet of pure liquid, thereby producing a larger radar cross section.

[21] The cirrus monthly mean cloud thickness is 1 km with a standard deviation from 600 m (dry season) to

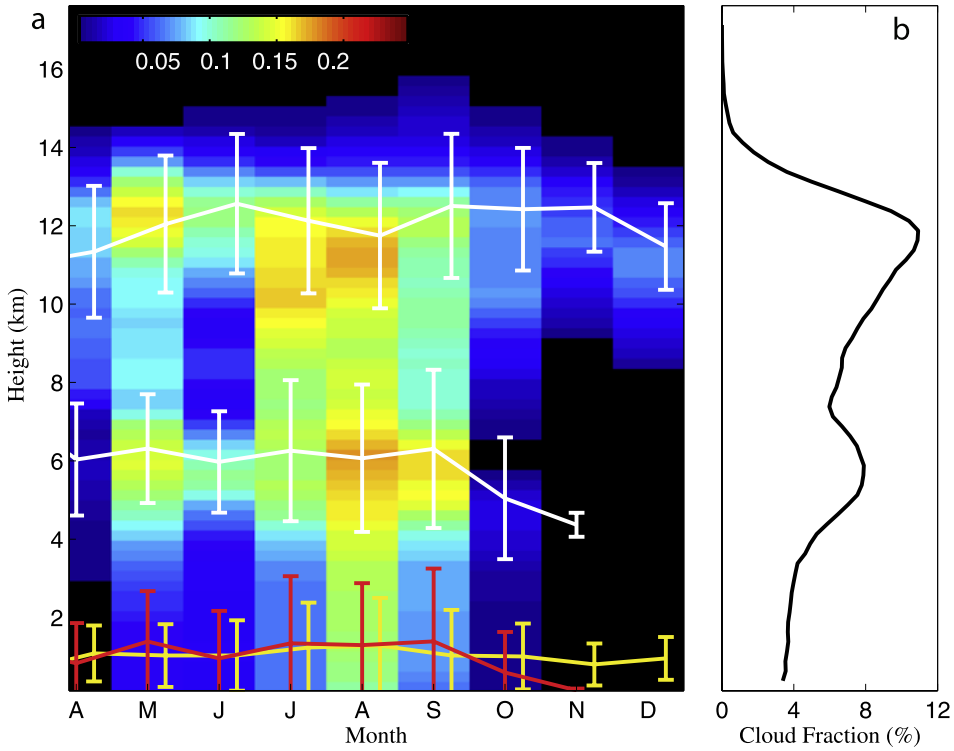

Figure 3. (a) Monthly averaged cloud and precipitation fraction. The monthly mean and standard deviation of cirrus cloud top (top white line), middle clouds tops (bottom white line), cirrus cloud thickness (yellow line), and middle clouds thickness (red line) are also shown. (b) The deployment-mean cloud and precipitation fraction during the AMF deployment at Niamey, Niger.

1500 m (wet season). The monthly averaged cirrus cloud top height varies from 11.5 to 12.5 km (Figure 3), although the small depression in the cirrus cloud top height observed in August is attributed to WACR attenuation. The monthly average midlevel cloud top height is 6 km during the wet season and the monthly averaged cloud thickness is 1 km (Figure 3).

[22] Precipitation is observed frequently during the wet season with typical events lasting approximately 2–6 h in the column sampled by the AMF WACR (Figures 4 and 1). Convective precipitation cores with rainfall rates > 10 mm h^{-1} and trailing stratiform precipitation are often observed (Figure 1). Other rainfall events appear to be associated exclusively with midlevel stratiform and cirrus clouds, perhaps because the convective core itself did not pass over the AMF site or the convective core was no longer active. The daily accumulated rainfall measured by a tipping bucket rain gauge at the AMF site is highly variable and there were 11 different days when 10 mm or more of accumulated rainfall was measured, 19 days with accumulated rainfall amount between 2 and 10 mm, and over 30 days with accumulated rainfall amounts of 0–2 mm (i.e., trace amount). The latter half of the monsoon period (August and beyond) is characterized by numerous days with small amounts of accumulated precipitation interspersed with strong convective rainfall events. In contrast, the earlier part of the monsoon period (before August) contains numerous events with medium amounts of accumulated precipitation and fewer strong convective events.

[23] Not all of the precipitation events observed by the WACR just above the surface resulted in measurable precipitation at the surface (Figure 4). In these instances, the surface rainfall rate was immeasurable by the tipping bucket rain gauge (rainfall rate < 0.245 mm h^{-1}) while the radar reflectivity steadily increased with altitude from the lowest measurable range gate, just above the surface. This signature, which is due to raindrop evaporation, was present in approximately 50% of all cases in which the WACR detected precipitation echoes in the lowest altitude radar range gate mostly in association with the trailing stratiform regions of convective cores (Figures 4 and 1). The preponderance of this signature suggests that evaporation of falling precipitation may play an important role in the redistribution of energy within the vertical column above Niamey. Evaporation of falling precipitation redistributes heat in the column, but does not contribute to latent heating since the amount of heat released during condensation is balanced by the amount of cooling during evaporation.

3.2. Thermodynamic Environment

[24] Convection is the primary source of rainfall and cloud cover during the rainy season in West Africa. This convection is a consequence of the availability and realization of convective available potential energy (CAPE). The CAPE for each half-hour profile is computed from the profiles of equivalent potential temperature, θ_e, and the saturation equivalent potential temperature, θ_{es}, using

$$\mathrm{CAPE} = \int_{\mathrm{LFC}}^{\mathrm{EL}} \frac{g\left(\theta_{e[\max]} - \theta_{es}(z)\right)}{(1+\gamma)\bar{\theta}}\, dz, \qquad (1)$$

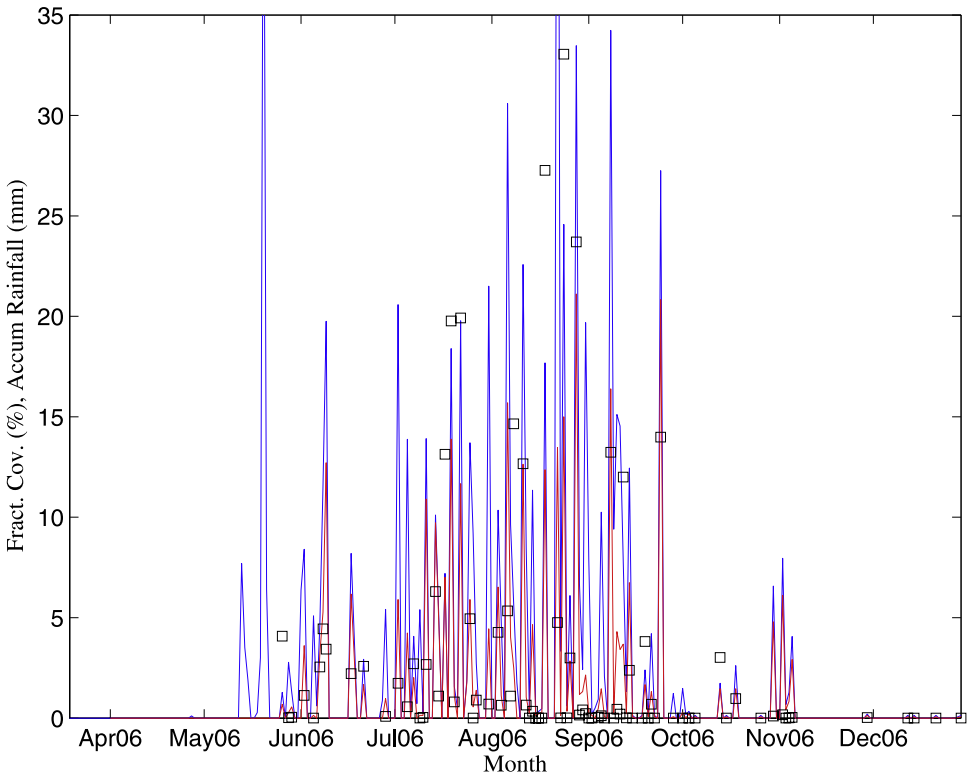

Figure 4. Daily observed fractional coverage of precipitation as identified from WACR echo (blue lines), accumulated daily rainfall (in millimeters, black squares), and observed fractional coverage of surface rainfall from a tipping bucket rain gauge (red lines). Note that the surface rainfall rate must exceed 0.245 mm h^{-1} (red lines) to be detectable using this rain gauge.

where LFC is the level of free convection, EL is the equilibrium level, g is gravity, $\theta_{e[max]}$ is the maximum value of the equivalent potential temperature in the profile, $\overline{\theta}$ is the mean potential temperature in the layer, and z is height. In (1), $\gamma = L^2 q_s (c_p R_v T^2)^{-1}$, where L is the latent heat of vaporization, q_s is the saturation specific humidity, c_p is the specific heat at constant pressure, R_v is the universal gas constant at constant volume, and T is temperature.

[25] In each thermodynamic profile, the largest value of θ_e in the column is taken as a reference point, $\theta_{e[max]}$, as illustrated with a blue asterisk just above 500 mbar in the profile in Figure 5a. This maximum is typically observed in the layer between the surface and 700 mbar, which is, interestingly, near the top of the semipermanent dust layer as measured using the MPL (not shown). Once this level is identified, the lowest value of θ_{es} in the layer above is located and recorded (black square in Figure 5a). If this value is not lower than the maximum θ_e, no CAPE is present and the profile is flagged accordingly. Otherwise, the level of free convection (LFC) is determined by locating the point on the θ_{es} profile above the θ_e maximum in which the values of the θ_e maximum and value θ_{es} are equivalent; this point is the bottom boundary of the CAPE integral (1). The top boundary is the point at which the maximum value of θ_e and θ_{es} are once again equal, which is defined as the equilibrium level (EL). This method of computing CAPE was selected because the complexity of the thermodynamic profiles made other approaches difficult to automate. This technique does have drawbacks in that it often overestimates the amount of CAPE [*Emanuel*, 1994], so vertical velocity estimates are also prone to overestimation and are avoided in this study. Despite its inclination to overestimate the actual magnitude of the CAPE, it is quite capable of portraying changes in CAPE.

[26] To illustrate some typical features of the thermodynamic and cloud structure for a typical convective event in the region, we selected a storm complex observed on 9 June 2006 for further investigation. During this event, convective rainfall commenced around 0700 UTC and ended around 1200 UTC, and prior to the event, there were no clouds detected for a period of hours. The prestorm and poststorm environments (Figures 5a and 5b) for this convective event show a considerable change in CAPE, represented by the positive area in the sounding in the prestorm environment and no CAPE in the poststorm profile. The CAPE in the prestorm environment exists for parcels above approximately 900 mbar, but is the largest and easiest to realize for parcels in the region around 700 mbar.

[27] The profile of θ_e in the prestorm environment shows significant layering and no well-mixed regions, which would have a constant value of θ_e as a function of pressure. This layering is indicative of a lack of convective overturning in the column prior to the onset of the convection. The prestorm profile of θ (Figure 5c) shows highly stable regions from the surface to 800 mbar and above 400 mbar with a less stable region between. After the storm passes, the θ_e profile shows considerably less layering and is nearly well-mixed (Figure 5b) in a region that is just above

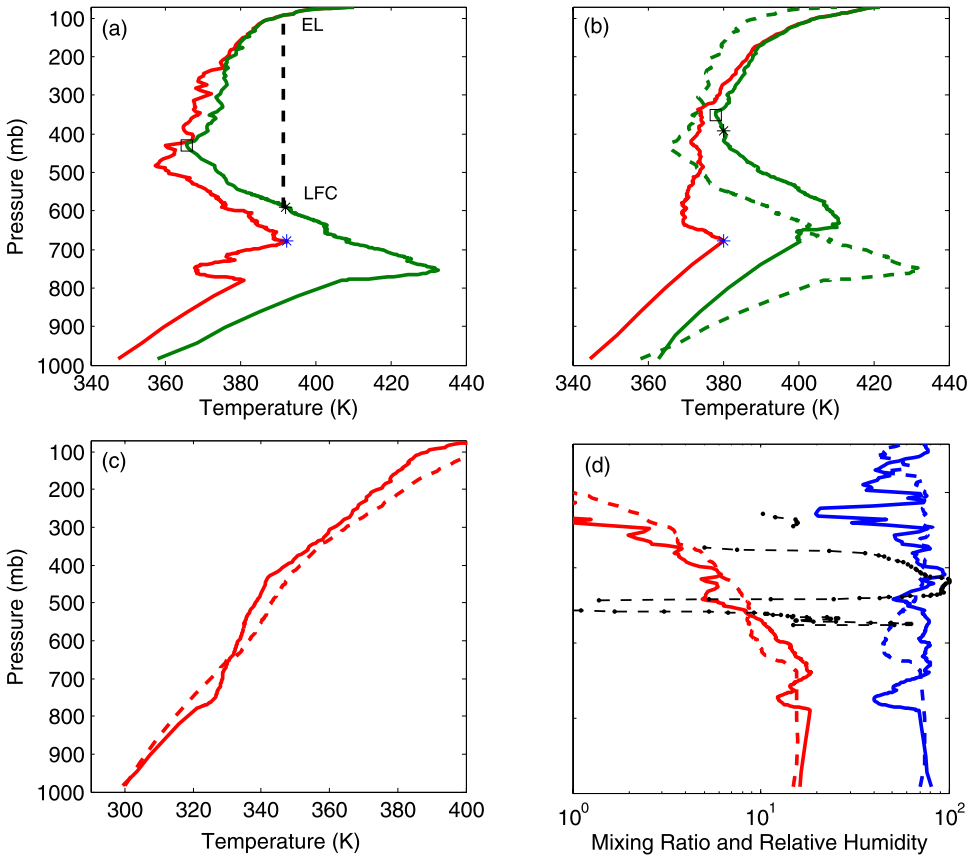

Figure 5. Prestorm (0500 UTC) and poststorm (1300 UTC) environments for 9 June 2006. (a) The equivalent potential (red line) and saturation equivalent potential temperatures (green line) for the prestorm environment. The level of free convection (LFC) and equilibrium level (EL) are indicated, and the blue asterisk and black square represent reference thermodynamic levels referred to in the text. The region bounded by the dashed black line and the green line is the positive area. (b) As in Figure 5a but for the poststorm environment. The dashed green line is the saturation equivalent temperature from the prestorm environment for reference. (c) The potential temperature profile for the prestorm (solid line) and poststorm (dashed line) environments. (d) The mixing ratio (red lines) and the relative humidity (blue lines) for the prestorm (solid lines) and poststorm (dashed lines) environments. The black dashed line with solid circles is the nonzero percent coverage of clouds in the poststorm environment.

the layer that was previously less stable between 800 and 400 mbar. Moisture was transported higher in the atmosphere as evidenced by the prestorm and poststorm specific humidity profiles (Figure 5d), while the relative humidity and cloudiness increased above 500 mbar. A rapid return to an environment that contained significant CAPE was observed within a few hours after the end of the rainfall associated with this event.

[28] An interesting characteristic of the convective environment observed at Niamey is that a maximum in θ_e is frequently observed in the vicinity of 700 mbar accompanied by a minimum in θ_{es} in the mid and upper troposphere. There is almost always considerable layering in the profile as would be expected if the air masses in different regions of the column had different points of origin and had been subjected to a range of different processes. Such structure is not atypical in environments that frequently experience strong convection, but the notable absence of well-mixed layers in most of the profiles is indicative of significant convective inhibition.

[29] To examine the evolution of the cloud, thermodynamic, and precipitation structure through the rainy season, a time series of key variables was constructed. Estimated thermodynamic profiles were available at 1-min intervals and cloud profiles at sub-1-min intervals. A one-half-hour averaging period was selected for the cloud profiles because experience has shown that the radiative impacts of the cloud field involve hemispheric contributions that are not well-characterized by single profiles of cloud structure from the relatively narrow column sampled by the WACR. There is no guarantee that these averages capture the hemispheric variability in the vicinity of Niamey, but they are superior to single samples or significantly longer averaging periods that smear details. The thermodynamic profile at the center time of each half-hour bin was recorded and interpolated to be consistent with the height-resolution of the WACR.

[30] A 6-day running-mean value of the time series of CAPE for the period encompassing the summer monsoon shows that CAPE is first observed in early May and quickly ramps to a value of approximately 5000 J kg^{-1} where it remains for the duration of the convective season

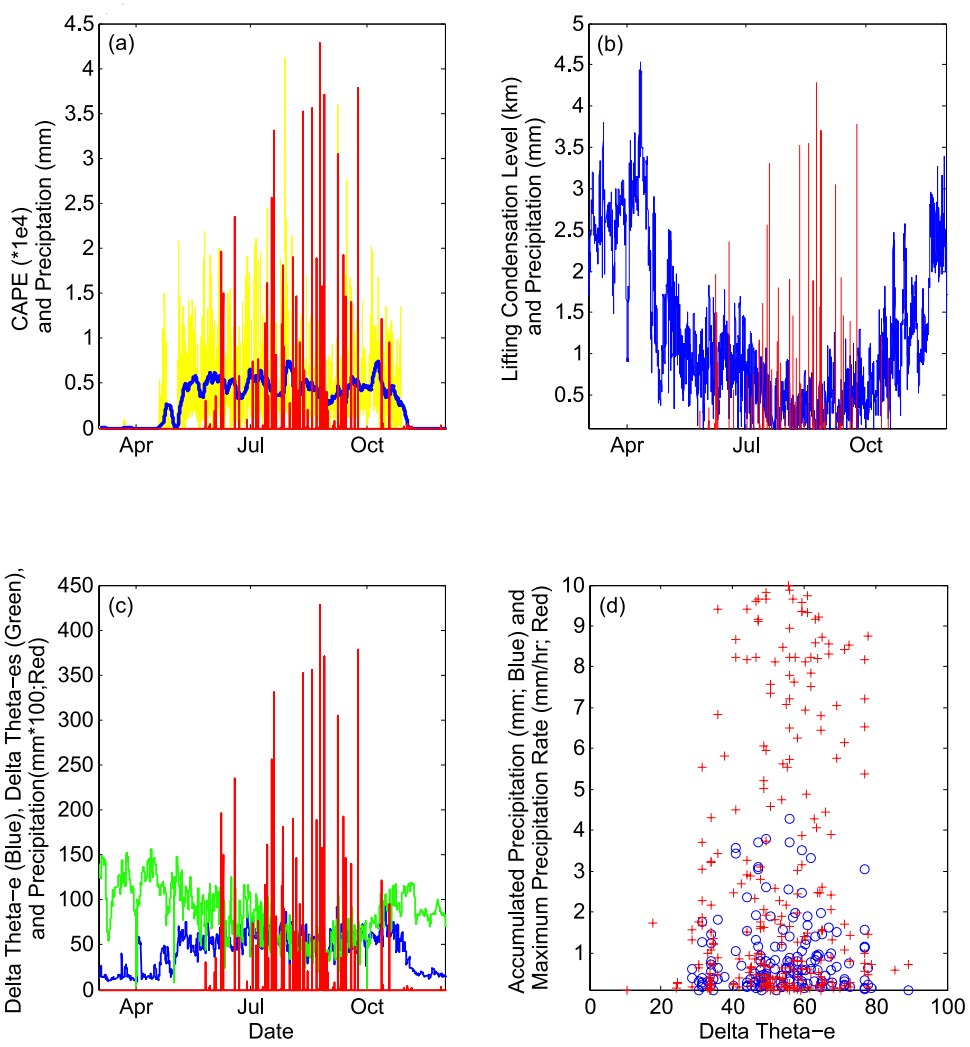

Figure 6. (a) The temporal relationship between CAPE and precipitation. The yellow line connects the half-hour estimations of CAPE, and the blue line is a running mean through the half-hour CAPE estimates. The red lines are half-hour accumulated precipitation. (b) The half-hour average lifting condensation level (blue line) versus half-hour accumulated precipitation (red lines). (c) The half-hour fluctuations in θ_e (blue line) and θ_{es} (green line) are plotted versus (red lines) half-hour accumulated precipitation. (d) The half-hour accumulated precipitation and precipitation rate (blue circles) is plotted versus half-hour fluctuations in θ_e (red crosses).

(Figure 6a). The 6-day averaging period is long enough to sample passing easterly waves and their surroundings. While the running-mean CAPE rarely exceeds 5000 J kg^{-1}, the instantaneous values can be much larger on occasion. Viewing the rainy season as a whole, CAPE remains relatively constant and does not appear to steadily increase with time as the monsoon evolves. There are also periods in which CAPE is quite large for a long period, but little or no precipitation is observed. Clearly, the relationship between CAPE and precipitation is tenuous during the rainy season of 2006.

[31] The soundings collected in Niamey were almost always conditionally unstable. Thus, the lifting condensation level (LCL) is a critical point in the column because saturation is required to realize the instability. The profile of the LCL for each half-hour profile was computed and the lowest value of the LCL above ground level was recorded (Figure 6b). Each point in the column possesses a unique LCL and, theoretically, the parcel requiring the least amount of lifting should be the initiation point of convection if the entire column is lifted by an equal increment. That said, the initial convection will induce further lifting in the layers below the initiation point and eventually the parcel with the LCL closest to the surface will become the cloud base. The LCL steadily declines from a level above 4 km in April to less than 0.5 km in the July through October period. A strong relationship between the LCL and accumulated precipitation is suggested and relationships between cloud cover, the LCL, and precipitation will be examined shortly.

[32] Details of the mixing processes that accompany convective overturning and the state of the vertical gradients in the lower atmosphere are revealed by analyzing half-hour

fluctuations in θ_e and θ_{es} at a specific level or at the surface (Figure 6c). These short-term fluctuations are generally a consequence of vertical mixing processes, whereas longer-term changes are ascribable to advection and radiation. Half-hour fluctuations in surface θ_e (and θ_{es}) were computed by subtracting the maximum and minimum values for each half-hour period.

[33] Coincident with the onset of the monsoon is a rapid increase in the half-hour fluctuations in θ_e, which are a consequence in changes in both moisture and temperature. This increase is indicative of mixing processes operating upon the increased vertical gradient in θ_e that is associated with the arrival of a cooler and moister air mass near the surface associated with the monsoon. Unlike the fluctuations in θ_e, which seem to ramp to a relatively constant value at the beginning onset of the monsoon, fluctuations in θ_{es}, which are driven entirely by the vertical temperature gradient, show a steady decrease associated with a steady reduction in the vertical temperature gradient as the monsoon proceeds. Thus, the increased fluctuations in θ_e at the onset of the monsoon appear to be associated with a substantial increase in the vertical moisture gradient, rather than a temperature gradient. The strong correlation between a steady reduction of the fluctuations in θ_{es}, which are associated with a reduction in the vertical temperature gradient, and the onset of precipitation suggests that the vertical temperature gradient (stability) plays a critical role in convective development, as expected.

[34] The impacts of precipitation-induced downdraft on the subcloud thermodynamic structure may be quantified through the detection and characterization of their signature in the time series of θ_e. Penetrating downdraft causes a change in surface θ_e, a conserved variable, as air from higher levels with different θ_e is transported to the surface, while precipitation that is not accompanied by downdraft will be accompanied by no perturbation in θ_e. Sorting the half-hour fluctuations in θ_e according to half-hour surface rainfall accumulation and rainfall rate reveals that all observed precipitation was accompanied by penetrating downdraft. Neither rainfall intensity nor half-hour rainfall accumulation showed any trend with respect to the magnitude of the observed perturbation in θ_e (Figure 6d), so the appearance and magnitude of penetrating downdrafts bears no relationship to the characteristics of the precipitation that reaches the surface.

[35] A monthly climatology of the cloud coverage and thermodynamic profiles was constructed to demonstrate the evolution during the rainy season. A 1-month time window was selected because longer-term averages tend to smear details owing to the migration of the ITCZ.

[36] The monthly averages of the cloud coverage profile (Figure 7) show the evolution of the cloud field from the onset through the end of the rainy season (May through October). The cloud coverage is characterized by recording the monthly mean as well as the maxima and minima in the half-hour averaged cloud coverage at each height during the month. The latter variable reveals layers that experienced no periods of complete overcast during the month. Separate peaks in the cloud fractional coverage and relative humidity are discernable in the lower and upper troposphere during May (Figure 7a) and there is a layer above 6 km that was not completely overcast at any time during this month (not shown). This lack of overcast implies that there were no convective events lasting more than one-half hour that filled the entire depth of the troposphere. In May, no appreciable precipitation was observed and the LCL is, on the average, just below 3 km.

[37] The ITCZ passes Niamey at the end of May as it migrates to the north. Separate peaks in the cloud fractional coverage in the vicinity of 5–6 km and above 10 km are still discernable in June, but less discernable in July through September. The peaks appear again with high fidelity at the conclusion of the monsoon in October (and November, which is not shown). The accumulated precipitation and precipitation intensity indices (calculation described shortly) are the largest in August, but are significant during the period of June through September, as previously noted. The LCL moves steadily closer to the surface as the summer progresses and appears to modulate the mean monthly storm accumulation and peak rainfall, as previously noted. The LFC also moves closer to the LCL, which increases the ease with which convection may realize the conditional instability that is present. The extremes in the relative humidity profile reveal that the variability in low-level relative humidity is significantly reduced at the height of the monsoon. Cloudiness that extends through the entire depth of the troposphere is observed throughout the monsoon season as indicated by the cloud frequency profiles; each layer experiences at least one half-hour period with complete overcast during this period (not shown). Despite this apparently cloudy environment, cloud fractional coverage remains modest in each individual layer (around 10% at the height of the monsoon).

[38] Unlike the LCL, which appears highly correlated with precipitation, the monthly mean CAPE shows only minor variation from May through October, as suggested in the time series analyzed previously. This suggests that there is significant CAPE most of the time, a thought that is reinforced by the rapid recovery of the atmosphere after the convective event on 9 June (Figure 5). Despite a noticeable increase in the relative humidity in the lowest levels of the troposphere, the temperature difference between θ_e and θ_{es} in the profiles remains relatively constant from month to month as does the difference in temperature between the maximum θ_e in the profile and the minimum θ_{es} above, which is related to the amount of CAPE.

[39] The association between cloud coverage and the freezing level has been documented in tropical regions [*Johnson et al.*, 1996; *Mather et al.*, 1998; *Johnson et al.*, 1999] and the monthly profiles from Niamey are no exception. There is a maximum at or just above the zero degree isotherm in the monthly profiles of cloud frequency in each of the 7 months examined in this study. The thermodynamic profiles also show a clear pivot at the freezing level. The minimum observed θ_e in the monthly mean also shows a sharp minimum at the freezing level.

[40] Withdraw of the monsoon layer raises the LCL and is associated with increasing intrusions of dry air at midlevels [*Numaguti et al.*, 1995; *Yoneyama and Parsons*, 1999] as evidenced by a noticeable minimum in the mean relative humidity in October and November (not shown). These features conspire to attenuate convection [*Brown and Zhang*, 1997; *Johnson et al.*, 1999; *Redelsperger et al.*, 2002; *Jensen and Del Genio*, 2006], which leads to the

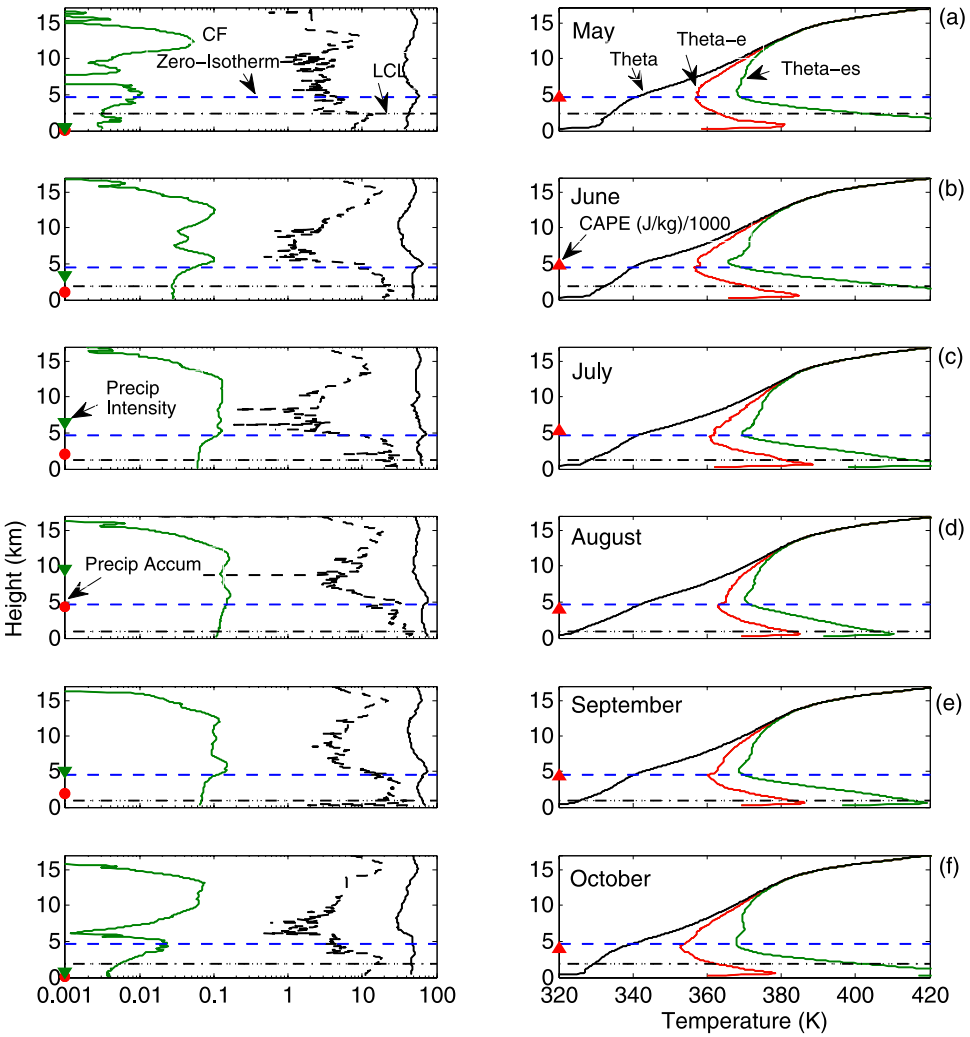

Figure 7. (left) Monthly mean profiles of cloud fractional coverage (green line), relative humidity (black line), minimum relative humidity and maximum relative humidity envelope (black dashed line to left of solid black line) for the months of May through October. The monthly Precipitation Accumulation Index (millimeters) is indicated with the solid red circle on the height axis, and the monthly Precipitation Intensity Index (mm/h) is indicated with the inverted green triangle. (right) Monthly mean profiles of θ (black solid line), θ_e (red line), θ_{es} (green line), and minimum θ_e (black dashed line) and the monthly mean CAPE/1000 (J kg^{-1}). The blue dashed line in each plot is the mean monthly level of the zero-degree isotherm, and the black dash-dotted line is the height of the LCL.

discrimination of separate peaks in the cloud coverage frequency profiles in the lower and upper troposphere. By November, extreme drying in the lower half of the column associated with injections of the Saharan air layer is apparent, and accordingly, CAPE is diminished and precipitation ceases.

[41] The sensitivity of the Sahel and West Africa to precipitation is well known and these data demonstrate some important functional relationships. An elevated level of cloudiness frequency through the depth of the troposphere is a good indicator of convective activity, so the sum of the mean fractional cloudiness over all 265 20-m-deep layers is used as a total column cloudiness index for the purpose of testing the relationships between cloud cover, precipitation, and the LCL height (Figure 8).

[42] Daily and monthly means of the half hour of this cloudiness index were computed along with daily and monthly means of the height of the LCL and two indices related to the magnitude and intensity of precipitation. A precipitation accumulation index was formulated by computing the monthly and daily means of the half-hour measurements of accumulated precipitation from a tipping bucket rain gauge. This measure is favored over a summation in that it produces an estimate of the amount of accumulated precipitation that would be observed if all convective rainfall events during the averaging period produced the same quantity of precipitation. A precipitation intensity index was formulated by recording the maximum rainfall rate during each half-hour period and computing daily and monthly means from these data. This measure quantifies the maximum intensity of precipitation that

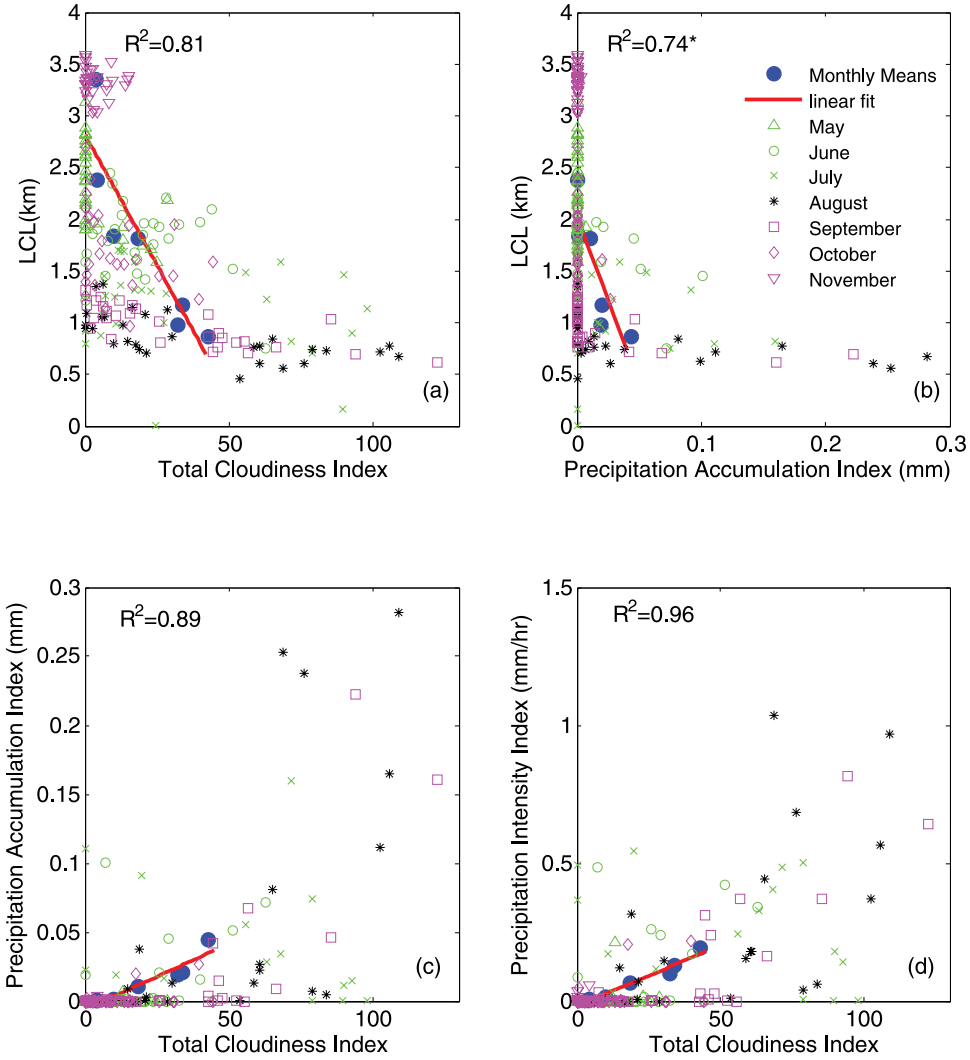

Figure 8. (a) The daily and monthly mean lifting condensation level (kilometers) versus the Total Column Cloudiness Index. The daily means for each month are plotted according to the legend shown in Figure 8b, and the monthly means are denoted with larger, solid blue circles. A linear fit to the monthly means is indicated with the solid red line and the amount of the variance explained by the fit (R^2) is also plotted. (b) As in Figure 8a but for the lifting condensation level (kilometers) versus a precipitation accumulation index (millimeters). The asterisk denotes the exclusion of November and inclusion reduces R^2 for the LCL height to 0.62. (c) As in Figure 8a but for the precipitation accumulation index versus the Total Column Cloudiness Index. (d) As in Figure 8a but for a Precipitation Intensity Index versus the Total Column Cloudiness Index.

would be observed if all convective events produced the same rainfall intensity.

[43] The monthly means of the LCL, precipitation accumulation index, and precipitation intensity index are strongly correlated with the monthly mean cloudiness index (R^2 = 0.81, 0.89, and 0.96; Figures 8a–8c). Strong correlations between the latter two variables and cloud cover are somewhat expected, but provide reassurance as to the self-consistency of the data set. The monthly mean LCL height is also strongly correlated with the monthly mean precipitation accumulation index (R^2 = 0.62), though if November, which is in the dry season, is excluded this correlation is significantly increased (R^2 = 0.74). No correlation is found between monthly mean CAPE and the monthly mean precipitation accumulation index (R^2 = 0.04). The daily values of the cloudiness index that underlie the monthly means show considerable scatter that is maximized at the height of the monsoon (August). The scatter in the daily total cloudiness index, for example, indicates interspersed cloudy, rainy, and clear days in August and only one third of the month has an elevated cloudiness index relative to those found during other months. The same configuration is seen in the daily precipitation accumulation index when plotted against the LCL (Figure 8b), and is also seen when the precipitation intensity index is plotted against LCL (not shown). As the LCL lowers, cloudiness throughout the column increases and the average convective cell produces more accumulated precipitation at the surface, which is delivered via a higher rainfall rate.

[44] Maximum utility of the vertical profiles of thermodynamic and cloud structure observed by the AMF requires that the columnar measurements be linked to larger atmospheric scales. In particular, the relationship between the observed cloud structure and the diagnosed regional vertical velocity is critical. Toward this end we employ initialization data from the National Center for Environmental Prediction's (NCEP) Global Forecast System (GFS) Atmospheric Model [*Kalnay et al.*, 1990; *Kanamitsu et al.*, 1991] because it represents one "best guess" at the diagnosed regional atmospheric structure over West Africa during the 2006 monsoon season. The GFS model initialization data set is formulated from an assimilation of multiple data sources including mandatory-level radiosonde data, satellite retrievals of temperature, satellite derived cloud motion vectors, aircraft, buoys, and ship observations [*Kanamitsu*, 1989]. Comparisons with the AMF data in this data sparse area present an opportunity to evaluate the efficacy of the GFS assimilated fields, while coincidently placing the AMF measurements in a regional context.

[45] The GFS assimilation produces estimates of the cloud and thermodynamic profiles with a horizontal resolution of 0.5 latitude $\times$ 0.5 degree longitude and vertical resolution that varies with height. The model contains 64 unequally spaced vertical levels and for a surface pressure of 1000 hPa, 15 levels are below 800 hPa, and 24 levels are above 100 hPa. The hypsometric relationship is used to convert the pressure level data to geopotential and the data for vertical profiles saved on standard heights (0–20 km at 250-m interval). Data from the grid cell containing the Niamey site are used in the comparisons that follow.

[46] June, August, and October were chosen for comparison because they represent the beginning, middle, and end of the monsoon season. The GFS horizontal wind components (Figure 9, left) show that most of the observed variability in the horizontal wind occurs in the east-west direction (u component), as would be expected for a tropical location. The wind profiles also reflect the passage of the ITCZ in May and in September, so the ITCZ is north of the AMF in June during the monsoon season. In October, upper-level westerlies replace the summertime easterlies. The u components for June and August show a strong easterly wind that deepens with time in the upper layers except in the shallow monsoon layer near the surface. Coincident with this deepening easterly flow is a large increase in cloud fraction through at least 10 km.

[47] The GFS vertical velocity profile shows low-level upward motion in June in the layer between the surface and 5 km, which corresponds quite well with an observed peak in the cloud fraction at the top of this layer (Figure 9, right). A similar couplet (upward motion and peak in the cloud fraction above) is observed in the vicinity of 10 km. These data suggest that at the onset of the monsoon, there is strong lifting in the lower levels of the atmosphere, likely associated with the passage of the ITCZ, which appears to be associated with maxima in cloud fraction. Correspondence between diagnosed upward motion and the vertical profile of cloud fraction exists is vague in August and October. At the end of the monsoon in October, vertical velocities in the layer below 5 km increase, but there is less coherence with the AMF-measured profile of cloud fraction. In summary, the structure of the AMF cloud fraction profile bears considerable correspondence to the vertical velocity diagnosed in the GFS at the beginning of the monsoon (June), but little correspondence during the height of the monsoon (August) and at its conclusion (October).

[48] Comparisons of the mean temperature profile from the AMF radiosondes and the GFS initialization show nearly perfect agreement, while comparisons of the profiles of relative humidity show important differences (Figure 10, left). The GFS initialization overestimates the relative humidity above 10 km for all three months and underestimates it in the monsoon layer near the surface. This result must be interpreted with some caution as the RS-92 radiosondes used in this study are known to have a dry bias in the upper atmosphere, particularly during the day, though it is unlikely that the entire magnitude of the discrepancy could be explained by this bias. The AMF and GFS initializations agree well in the middle levels of the atmosphere, though the GFS appears too moist in the layer between 2 and 5 km in October (Figure 10e).

[49] Profiles of cloud fraction produced in the GFS initialization and measured by the AMF WACR are considerably different. The GFS diagnoses too few clouds in June and too many in October, but has the least correspondence with the AMF-measured profile of cloud fraction during the height of the monsoon (Figure 10d). Much of the cloud information in the GFS initialization is derived from satellite and during the apex of the monsoon, when there is a preponderance of deep convective clouds, it seriously underestimates the amount of cloud below 10 km and may overestimate the amount of cloud above 10 km. Caution must be exercised when comparing clouds above 10 km with the AMF WACR owing to the potential impacts of attenuation.

4. Summary and Discussion

[50] Combining the WACR, MPL, ceilometers, radiosonde, and surface meteorological observations we develop vertically resolved cloud statistics for the 1-year-long Niamey, Niger deployment of the AMF and analyze them in the context of the thermodynamic environment and precipitation. The analysis spans the dry and wet (monsoon) seasons. The dry season (October to April) is characterized by persistent tropical cirrus of approximately 20% average coverage and 1-km thickness. This cirrus is characterized by bursts that take the form of peaks in the cloud frequency, which last on the order of a few days, surrounded by periods with little or no cirrus. Frequent dust outbreaks were observed during the dry season [*Slingo et al.*, 2006] and boundary layer and middle layer clouds are rarely observed. The dryness of the Saharan air masses in the lower levels is the likely cause of attenuated boundary layer cloudiness. The wet season (May to September) is characterized by intermittent convection of varying intensity that produces several hours of precipitation on some days and other days with no precipitation.

[51] It is difficult to usefully compare observations from a single point with regional composite structures computed by models, so we do so with some trepidation and only in generalities. The surface values of θ_e appear roughly consistent with those of *Hodges and Thorncroft* [1997], which are derived from ECMWF data, though the large

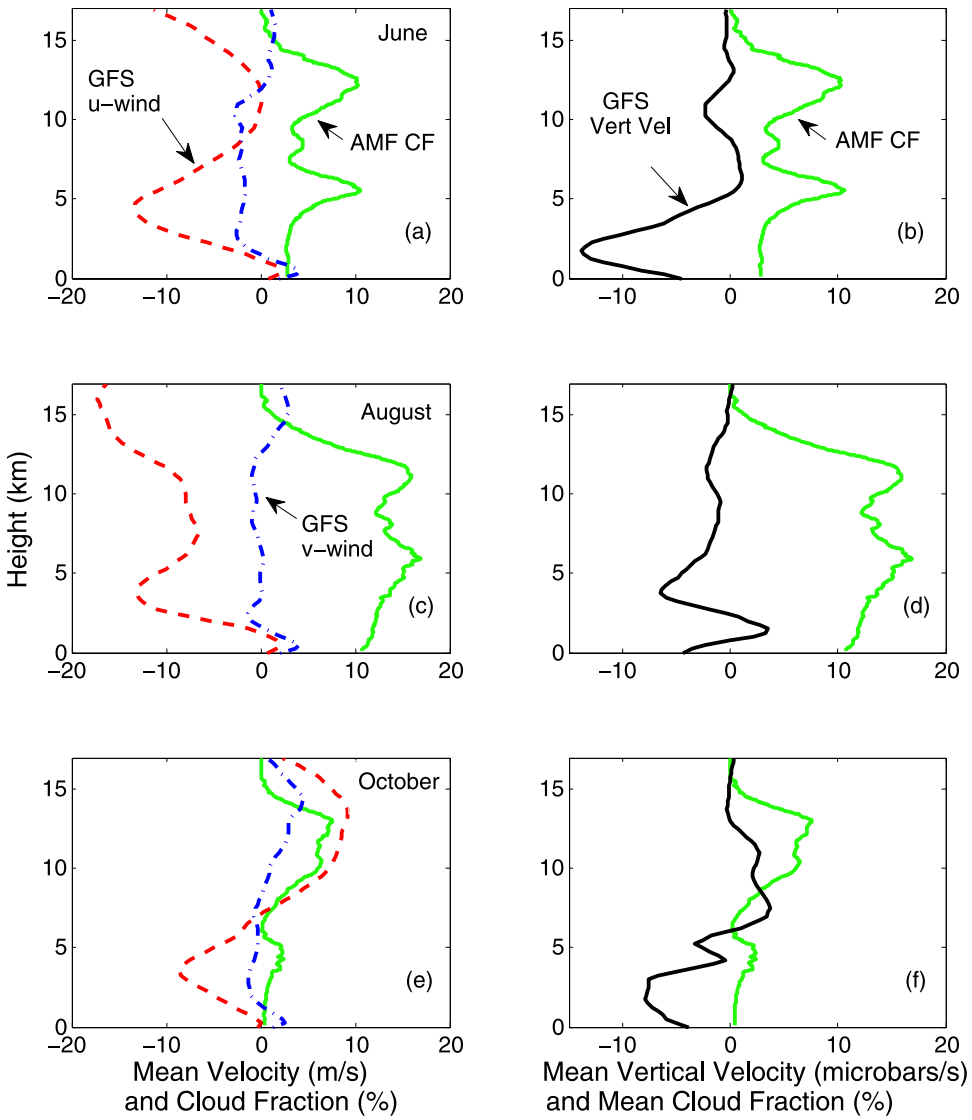

Figure 9. Comparisons of AMF mean cloud fraction (%) as a function of height with initialization data used in the NCEP GFS model for the months of (a and b) June, (c and d) July, and (e and f) October. (left) The mean u component (red dashed line) of the horizontal wind (m/s), the mean v component (blue dash-dotted line) of the horizontal wind (m/s), and the mean AMF cloud fraction (%; green solid line). (right) The mean vertical velocity in units of μbars s^{-1} (black line) and the mean AMF cloud fraction (%; green line).

vertical gradient and sharp peak in θ_e observed in the present study during the rainy season is not well represented. The location of this maximum in θ_e is often coincident with the top of the dust layer, as measured with the MPL, so we conjecture that its occurrence at this level could be related to radiative processes associated with the thick dust and aerosol layer. We also observed a minimum in θ_{es} is the midlevels that appear inconsistent with the ECMWF rainy season cross sections. While these are noteworthy observations, a more appropriate comparison would utilize regional radiosonde data, which is beyond the scope of this study.

[52] The rainy season is predicated upon the continuous availability of CAPE. The values of CAPE that we estimate ($\sim$5000 J kg^{-1}) are substantially larger than those found by *Monkam* [2002] (2000 J kg^{-1}), most likely because (1) our method tends to exaggerate the absolute amount of CAPE because we determine its value from the parcel with the maximum positive area, (2) we use a conservative variable approach that employs equivalent potential temperatures, and (3) the data set analyzed by *Monkam* [2002] uses only low-resolution data from mandatory levels, which may underestimate the maximum CAPE given the sharp vertical gradients that are observed in our data. The true mean value of CAPE in this region probably lies between these two extremes.

[53] Despite the availability of this CAPE to fuel convection, no substantial relationship between the amount of CAPE, cloudiness, and precipitation exists in these data. This is consistent with *Sherwood* [1999], who showed that although there is a minimum amount of CAPE necessary for convection to occur in the tropics, increased CAPE does not

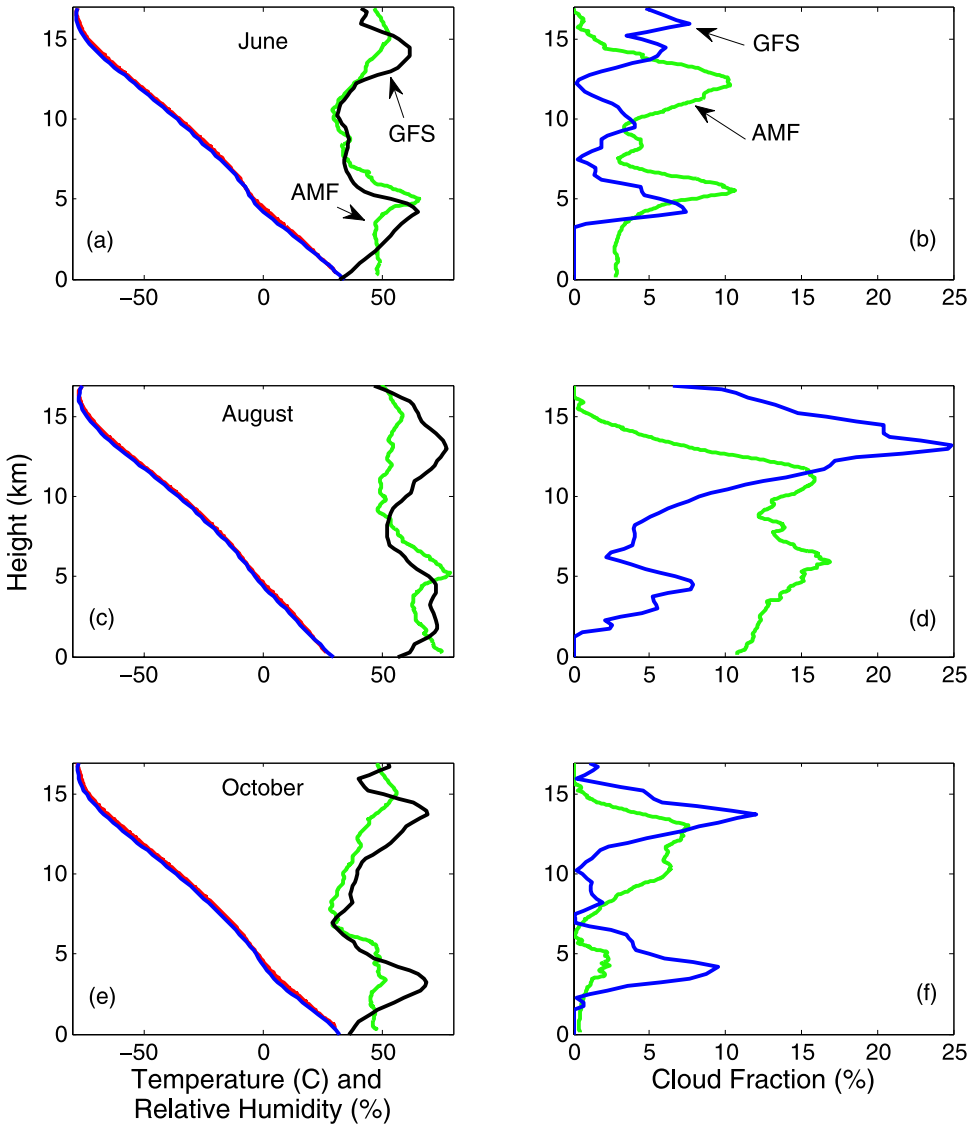

Figure 10. Comparisons of AMF mean temperature (K), relative humidity (%), and cloud fraction (%) as a function of height (kilometers) with initialization data used in the NCEP GFS model for the months of (a and b) June, (c and d) July, and (e and f) October. (left) Temperature (K) from the AMF (red line) and the NCEP GFS initialization (blue line), and the relative humidity (%) from the AMF (green line) and NCEP GFS initialization (black line). (right) AMF cloud fraction in % (green line) and the NCEP GFS initialization (blue line).

necessarily result in more vigorous convection. *Jensen and Del Genio* [2006] also show only a weak correlation between the magnitude of CAPE and convective cloud top heights in the tropical western Pacific. Our results show lower correlation between CAPE and precipitation than found by *Monkam* [2002], though both studies show relatively weak relationships between the two variables.

[54] The occurrence of deep convection and its accompanying rainfall is best correlated with a reduction in the height of the LCL and an accompanying reduction in the height of the LFC, which enhances the probability of cloud development in the observed conditionally unstable environment. Lowering of the LFC also changes the distribution of positive area in a manner that provides more buoyancy at lower levels. Changes in the structure of the temperature profile in the lower troposphere correspond with the occurrence of convection and precipitation. The observed decrease in the LCL and LFC are, to a large extent, modulated by cooling of the lower troposphere while the integrated amount of moisture remains relatively constant.

[55] The discordance in the time series of θ_e and that of θ_{es}, suggests that a steady reduction in the vertical temperature gradient in the lower troposphere is primarily responsible for the observed decrease in the LCL and the realization of CAPE. At the height of the monsoon, the θ_e and θ_{es} fluctuations are roughly equal. One explanation for this agreement is that temperature profile is modulating the profile of θ_e, while the moisture profile remains relatively constant. Examination of the soundings suggests that the

approximately 50 K fluctuations in θ_e are a result of mixing through the layer between the surface and 700 mbar. This is approximately the level of maximum θ_e in the column, so the convection is serving to reduce the vertical gradients in the lower troposphere as expected.

[56] A salient aspect of many of the thermodynamic profiles and accompanying cloud structure examined is significant layering. The lower 300 mbar of the troposphere was, by and large, more stable than the midlayers. Well-mixed layers are rarely observed. While the causes of this layering probably involve a complex variety of processes, it contributes significantly to the observed cloud and thermodynamic structure.

[57] Like many tropical regions, the zero-degree isotherm is intimately related to the vertical structure of cloudiness and to structural changes in the thermodynamic profile itself. A maximum in cloudiness is always observed at or just above the zero degree isotherms during the monsoon season and monthly mean values of θ_e and θ_{es} show a sharp minimum at this level. A particularly interesting association between the maximum observed θ_e during each month and the zero degree isotherms is present in these data. The causes of these significant changes in the vertical structure of the column are apparently related to the change in phase of precipitation. There are several potential explanations for the observed sensitivity of the tropical atmosphere to the location of the zero-degree isotherm. One explanation is that the temperature of the condensate must remain constant through the depth of its change of phase. This cold condensate is falling into a warmer and moister layer and it may physically cool the layer. This would result in the observed increase in relative humidity, decrease in temperature, and increase in cloudiness due to additional cooling of nearly saturated moist air. Another explanation is that newly glaciated particles are detrained from the main body of the cloud owing to aerodynamics and advected laterally where they are subsequently evaporated. Whatever the combination of processes that produces the observed minima at the freezing level, it is clear that condensate freezing and melting is substantially correlated with the thermodynamic profile in West Africa.

[58] The omnipresence of CAPE during the rainy season and the relationship between rainfall occurrence and the height of the LCL exposes some potential local mechanisms that could alter the occurrence of rainfall in the region. Mechanisms that cool or further moisten the lowest levels of the troposphere could impact the precipitation process, assuming that the data set considered here is representative.

[59] Comparisons with the NCEP GFS initialization data, which is derived from a number of sources including satellites, show some systematic biases when compare to AMF measurements. There is reasonable correspondence between the locations of clouds as measured by the AMF and the profile of vertical velocity diagnosed by the GFS initialization at the onset of the monsoon (June), but vague correspondence thereafter. The relative humidity in the GFS initialization is too large above 10-km and too small in the monsoon layer near the surface. Most importantly, the GFS initialization seriously underestimates the amount of cloud below 10 km during the height of the West African monsoon in Niamey. It may also overestimate the amount of high cloud during this period, but this result is less definitive owing to potential instrument bias. This analysis highlights the difficulty in obtaining reliable estimates of the large-scale thermodynamic and cloud structure in West Africa. The GFS diagnosed structure appears to have shortcomings due to the sparseness of data and complications with satellite retrievals at the height of the monsoon. These are expected in such a challenging environment and the results of this study imply that improved assimilations may be an important step toward improving weather and climate forecasts in this sensitive region.

[60] **Acknowledgments.** The lead and second author wish to dedicate their work on this paper to the memory of Anthony Slingo, who was our friend and colleague. Many dedicated professionals have contributed to the design, construction, and deployment of the ARM Mobile Facility. Mike Alsop, Betsy Andrews, Mary Jane Bartholomew, Dick Egan, Larry Jones, Kim Nitschke, John Ogren, Rex Pearson, Doug Sisterson, Jimmy Voyles, and Kevin Widener have made notable contributions.

References

Brown, R. G., and C. Zhang (1997), Variability of mid-tropospheric moisture and its effect on cloud-top height distribution during TOGA-COARE, *J. Atmos. Sci.*, *54*, 2760–2774, doi:10.1175/1520-0469(1997)054<2760:VOMMAI>2.0.CO;2.

Charney, J. G. (1975), Dynamics of deserts and droughts in the Sahel, *Q. J. R. Meteorol. Soc.*, *101*, 193–202, doi:10.1002/qj.49710142802.

Clothiaux, E. E., T. P. Ackerman, G. G. Mace, K. P. Moran, R. T. Marchand, M. A. Miller, and B. E. Martner (2000), Objective determination of cloud heights and radar reflectivities using a combination of active remote sensors at the ARM CART Sites, *J. Appl. Meteorol.*, *39*, 645–665, doi:10.1175/1520-0450(2000)039<0645:ODOCHA>2.0.CO;2.

Comstock, J. M., T. P. Ackerman, and G. G. Mace (2002), Ground-based lidar and radar remote sensing of tropical cirrus cloud at Nauru Island: Cloud statistics and radiative impacts, *J. Geophys. Res.*, *107*(D23), 4714, doi:10.1029/2002JD002203.

Cook, K. H. (1999), Generation of the African easterly jet and its role in determining West African precipitation, *J. Clim.*, *12*, 1165–1184.

Desbois, M., T. Kayiranga, B. Gnamien, S. Guessous, and L. Picton (1988), Characterization of some elements of the Sahelian climate and their interannual variations for July 1983, 1984, and 1985 from the analysis of METEOSAT ISCCP data, *J. Clim.*, *1*, 867–904, doi:10.1175/1520-0442(1988)001<0867:COSEOT>2.0.CO;2.

Emanuel, K. A. (1994), *Atmospheric Convection*, 580 pp., Oxford Univ. Press, Oxford, U. K.

Frisch, A. S., C. W. Fairall, and J. B. Snider (1995), Measurement of stratus cloud and drizzle parameters in ASTEX with a K_a-band Doppler radar and a microwave radiometer, *J. Atmos. Sci.*, *52*, 2788–2799, doi:10.1175/1520-0469(1995)052<2788:MOSCAD>2.0.CO;2.

Harries, J. E., et al. (2005), The Geostationary Earth Radiation Budget (GERB) Experiment, *Bull. Am. Meteorol. Soc.*, *86*, 945–960, doi:10.1175/BAMS-86-7-945.

Hodges, K. I., and C. D. Thorncroft (1997), Distribution and statistics of African mesoscale convective weather systems based on the ISCCP Meteosat imagery, *Mon. Weather Rev.*, *125*, 2821–2837, doi:10.1175/1520-0493(1997)125<2821:DASOAM>2.0.CO;2.

Jensen, M. P., and A. D. Del Genio (2006), Factors limiting convective cloud top height at the ARM Nauru Island climate research facility, *J. Clim.*, *19*, 2105–2117, doi:10.1175/JCLI3722.1.

Jensen, M. P., and D. Troyan (2006), Continuous water vapor profiles for the fixed atmospheric radiation measurement sites: 2006 ARM Metric first quarter report, *DOE/SC-ARM/P-06–002*, 6 pp., U.S. Dep. of Energy., Washington, D. C.

Johnson, R. H., P. E. Ciesielski, and K. H. Hart (1996), Tropical inversions near the 0°C level, *J. Atmos. Sci.*, *53*, 1838–1855, doi:10.1175/1520-0469(1996)053<1838:TINTL>2.0.CO;2.

Johnson, R. H., T. M. Rickenbach, S. A. Rutledge, P. E. Ciesielski, and W. H. Shubert (1999), Trimodal characteristics of tropical convection, *J. Clim.*, *12*, 2397–2418, doi:10.1175/1520-0442(1999)012<2397:TCOTC>2.0.CO;2.

Kalnay, E., M. Kanamitsu, and W. E. Baker (1990), Global numerical weather prediction at the National Meteorological Center, *Bull. Am. Meteorol. Soc.*, *71*, 1410–1428, doi:10.1175/1520-0477(1990)071<1410:GNWPAT>2.0.CO;2.

Kanamitsu, M. (1989), Description of the NMC global data assimilation and forecast system, *Weather Forecast.*, *4*, 335–342, doi:10.1175/1520-0434(1989)004<0335:DOTNGD>2.0.CO;2.

Kanamitsu, M., J. C. Alpert, K. A. Campana, P. M. Caplan, D. G. Deaven, M. Iredell, B. Katz, H.-L. Pan, J. Sela, and G. H. White (1991), Recent changes implemented into the global forecast system at NMC, *Weather Forecast.*, *6*, 425–435, doi:10.1175/1520-0434(1991)006<0425:RCIITG>2.0.CO;2.

Laing, A. G., and J. M. Fritsch (1993), Mesoscale convective complexes in Africa, *Mon. Weather Rev.*, *121*, 2254–2263, doi:10.1175/1520-0493(1993)121<2254:MCCIA>2.0.CO;2.

Lamb, P. J. (1978), Case studies of tropical Atlantic surface circulation patterns during recent sub-Saharan weather anomalies: 1967 and 1968, *Mon. Weather Rev.*, *106*, 482–491, doi:10.1175/1520-0493(1978)106<0482:CSOTAS>2.0.CO;2.

Lebel, T., J.-L. Redelsperger, and C. Thorncroft (2003), African Monsoon Multidisciplinary Analysis (AMMA) Project, *GEWEX News*, *13*(4), 8–9.

Mather, J. H., M. P. Jensen, and T. P. Ackerman (1998), Characteristics of the atmospheric state and the surface radiation budget at the tropical western Pacific ARM site, *Geophys. Res. Lett.*, *25*, 4513–4516, doi:10.1029/1998GL900196.

Miller, M. A., and A. Slingo (2007), The Atmospheric Radiation Measurement (ARM) Mobile Facility (AMF) and its first international deployment: Measuring radiative flux divergence in West Africa, *Bull. Am. Meteorol. Soc.*, *88*, 1229–1244, doi:10.1175/BAMS-88-8-1229.

Monkam, D. (2002), Convective available potential energy (CAPE) in northern Africa and tropical Atlantic and study of its connections with rainfall in central and West Africa during summer 1985, *Atmos. Res.*, *62*, 125–147, doi:10.1016/S0169-8095(02)00006-6.

Numaguti, A., R. Oki, K. Nakamura, K. Tsuboki, N. Misawa, T. Asai, and Y.-M. Kodma (1995), 45-day-period variation and low-level dry air observed in the equatorial western Pacific during TOGA COARE, *J. Meteorol. Soc. Jpn.*, *73*, 267–290.

Otterman, J. (1974), Baring high-albedo soils by overgrazing: A hypothesized desertification mechanism, *Science*, *186*, 531–533, doi:10.1126/science.186.4163.531.

Redelsperger, J.-L., D. B. Parsons, and F. Guichard (2002), Recovery processes and factors limiting cloud-top height following the arrival of a dry intrusion observed during TOGA COARE, *J. Atmos. Sci.*, *59*, 2438–2457, doi:10.1175/1520-0469(2002)059<2438:RPAFLC>2.0.CO;2.

Sherwood, S. C. (1999), Convective precursors and predictability in the tropical western Pacific, *Mon. Weather Rev.*, *127*, 2977–2991, doi:10.1175/1520-0493(1999)127<2977:CPAPIT>2.0.CO;2.

Slingo, A., et al. (2006), Observations of the impact of a major Saharan dust storm on the Earth's radiation budget, *Geophys. Res. Lett.*, *33*, L24817, doi:10.1029/2006GL027869.

Thorncroft, C. D., and M. Haile (1995), The mean dynamic and thermodynamic fields for July 1989 over tropical north Africa and their relationship to convective activity, *Mon. Weather Rev.*, *123*, 3016–3031, doi:10.1175/1520-0493(1995)123<3016:TMDATF>2.0.CO;2.

Yoneyama, K., and D. B. Parsons (1999), A proposed mechanism for the intrusion of dry air into the tropical western Pacific region, *J. Atmos. Sci.*, *56*, 1524–1546, doi:10.1175/1520-0469(1999)056<1524:APMFTI>2.0.CO;2.

M. P. Jensen, K. L. Johnson, and D. T. Troyan, Department of Atmospheric Sciences, Brookhaven National Laboratory, 2 Center Street, Upton, NY 11973, USA.

P. Kollias, Department of Atmospheric and Oceanic Sciences, McGill University, 805 Sherbrooke Street West, Montreal, QC H3A 2K6, Canada. (pavlos.kollias@mcgill.ca)

M. A. Miller, Department of Environmental Sciences, Rutgers University, New Brunswick, NJ 08901, USA.